No excess of Star Formation in the $z = 1.4$ Structure:
Hα Observations of the Radio-loud AGN 6CE1100+3505 Field

Hyunjin Shim[1], Jong Chul Lee[2], Narae Hwang[2], and Byeong-Gon Park[2]

[1]Department of Earth Science Education, Kyungpook National University, 80 Daehakro, Bukgu, Daegu 41566, Korea;
hjshim@knu.ac.kr
[2]Korea Astronomy and Space Science Institute, Daejeon 34055, Korea

Abstract: We present the results of near-infrared imaging observations of the galaxy overdensity around the $z = 1.44$ radio-loud active galactic nucleus (AGN) 6CE1100+3505, which was carried out with the purpose of sampling the redshifted Hα emission from the actively star-forming galaxies that could constitute the overdensity. The existence of the structure around this AGN was spectroscopically confirmed by previous grism observations which are however limited to the central region. Using the CH4Off narrow/medium-band and H broad band filters in the Wide Infrared Camera (WIRCam) on the Canada-France-Hawaii Telescope (CFHT), we constructed a sample of objects that show a flux excess in the CH4Off band due to line emission. The emission line flux is $\sim 4.9 \times 10^{-16}$ erg s^{-1} cm^{-2}, corresponding to a star formation rate (SFR) of $\sim 50\,M_\odot$ yr^{-1} for galaxies at redshifts $z \sim 1.4$. None of the galaxies with medium-band flux excess is located within 1 Mpc from the central AGN, and there is no evidence that the selected galaxies are associated with the proposed cluster. Along with the star formation quenching near the center that was found from the previous grism observations, the lack of extreme starbursts in the structure suggests that at $z \sim 1.4$, overdense regions are no longer favorable locations for vigorous star formation.

Key words: galaxies: evolution — galaxies: clusters — galaxies: star formation

1. Introduction

Widely recognized morphology–density or color–density relations in the local Universe (Dressler 1980; Kauffmann et al. 2004) shaped the idea that galaxy clusters are the most massive structures populated mainly by quiescent galaxies. The fraction of star-forming galaxies is significantly lower in local clusters ($z < 0.1$) than in the field (Chung et al. 2011), no obscured star formation is found to be present in nearby clusters (Davies et al. 2010), and the star formation rate (SFR) from galaxies in clusters only accounts for $\sim 0.25\%$ of the global SFR density at $z \sim 0$ (Iglesias-Páramo et al. 2002). These observational results suggest that galaxy evolution is strongly affected by the environment.

Unlike in the local Universe, numerous clusters of galaxies at $z > 0.5$ show a significant number of star-forming galaxies with strong ongoing star formation. Infrared and submillimeter observations revealed heavily obscured star formation in massive clusters at $1 < z < 2$ (Bayliss et al. 2014; Ma et al. 2015; Stach et al. 2017). The fraction of star-forming galaxies in clusters is large compared to that in the field at the same redshift ($z = 1.6$, Santos et al. 2013; $z > 1.2$, Alberts et al. 2014). In some clusters, star-forming galaxies are observed to be more concentrated near the cluster center ($z = 1.4$, Hayashi et al. 2010; $z > 1.4$, Brodwin et al. 2013), showing a reversal of the morphology-density relation at high redshift (Elbaz et al. 2007). The total integrated SFR within the cluster normalized by the cluster mass,

i.e., the cluster-specific SFR, is found to be increasing steeply as the redshift increases up to $z \sim 2$, i.e., the peak of cosmic star formation (Geach et al. 2006; Bai et al. 2009; Ma et al. 2015). The (proto)clusters must have been a place for vigorous star formation in the early Universe.

At $z > 2$, galaxies with SFRs above $100\,M_\odot$ yr^{-1}, i.e., starburst galaxies, are found within the protoclusters and/or galaxy overdensities (e.g., Hatch et al. 2011; Cooke et al. 2014). Numerous works presenting the close connection between the submillimeter galaxies (SMGs) and the galaxy overdensity provide evidence that extreme starbursts might appear in the center of the most massive halo (e.g., Dannerbauer et al. 2014; Umehata et al. 2015). SMGs have thus been used as probes of massive structures in the early Universe (Clements et al. 2015). However, it has also been claimed that SMGs do not usually detect overdensities even though they trace dark matter halos better than star-forming galaxies such as Lyman break galaxies, mainly due to Poisson noise from small sample sizes (Miller et al. 2015). In any case, massive galaxy structures at $z > 2$ appear to be a favorable environment for galaxies with exceptionally strong ongoing star formation. Yet it is not clear where in the redshift range $1 < z < 2$ the most vigorously star-forming galaxies are located, while the works with dusty star-forming galaxies including SMGs are all focused on the study of $z > 2$ protoclusters.

Environmental effects on the star formation activity of galaxies in the redshift range $1 < z < 2$ are still a

Corresponding author: H. Shim

matter of debate. Recent studies tend to agree that the environmental effect on star formation 'quenching' becomes dominant over the internal mass-dependent quenching at $z \sim 1$ (Lee et al. 2015; Darvish et al. 2016). The paucity of star formation in local galaxy clusters is a natural consequence of such environmental quenching. Specifically, the onset of the locally observed morphology-density relation can be placed at $z \sim 1.5$, supported by the strong evolution of quenching efficiency at $0.9 < z < 1.6$ (Nantais et al. 2017), the evolution of star formation activity in clusters (Wagner et al. 2017), and the high fraction of quiescent galaxies in cluster cores at $z \sim 1.5$ (Strazzullo et al. 2019). From comparison of fractions of star forming galaxies and specific SFRs in clusters at $z > 1.4$ and $z < 1.4$, Brodwin et al. (2013) concluded that the transition from unquenched high-redshift clusters with high central SFRs to passive, star-formation quenched low-redshift clusters occurs at $z = 1.4$. These results are inconsistent with the observations of strongly star-forming galaxies at $1 < z < 2$ mentioned above; therefore it is worth investigating where all the strong star-forming galaxies at $1 < z < 2$ are, especially around a redshift of $z \sim 1.4$ that marks an important epoch for efficient environmental quenching.

In this paper, we discuss the properties of potential $z \sim 1.4$ Hα emitters in the region around the $z = 1.44$ radio-loud AGN 6CE1100+3505. Candidate sources are those that show higher fluxes in narrow/medium band than in broad band photometric filters. The $z \sim 1.4$ structure was identified as a probable cluster by spectroscopy (Noirot et al. 2018). By combining the available spectroscopic data for the cluster core ($< 500\,\mathrm{kpc}$) and newly obtained narrow/medium-band observations out to several times of the cluster size ($> 4\,\mathrm{Mpc}$), we derive the specific SFR of galaxies with strong Hα emission and check if these starbursts populate the confirmed structure. All magnitudes are given in the AB system unless stated otherwise. The cosmological parameters used are $H_0 = 71\,\mathrm{km\,s^{-1}}$, $\Omega_\mathrm{M} = 0.27$, and $\Omega_\Lambda = 0.73$.

2. DATA
2.1. Overdensity around the Radio-loud AGN

Our target field, the environment of the radio-loud AGN 6CE1100+3505 at $z = 1.44$, was initially selected based on the excess of *Spitzer* IRAC-selected sources within $\sim 1\,\mathrm{Mpc}$ found by a count-in-cell analysis in a deep IRAC imaging survey around $1 < z < 3$ radio galaxies (Clusters Around Radio-Loud AGN program for *Spitzer*; Wylezalek et al. 2013). The H$^-$ $1.6\,\mu\mathrm{m}$ bump in the spectral energy distribution of galaxies can be used for estimating photometric redshifts regardless of the galaxy type (Sawicki 2002). The $1.6\,\mu\mathrm{m}$ bump is redshifted into the IRAC ch2 band ($\lambda_\mathrm{cen} \simeq 4.5\,\mu\mathrm{m}$) at $z > 1.3$; more than 80% of sources with IRAC color $[3.6\,\mu\mathrm{m}] - [4.5\,\mu\mathrm{m}] > -0.1$ are indeed located at $z > 1.3$ (Papovich et al. 2007; Wylezalek et al. 2013). The surface number density of sources with red IRAC color (i.e., $[3.6] - [4.5] > -0.1$) around 6CE1100+3505 is $\sim 21\,\mathrm{arcmin^{-2}}$, which is more than $3\,\sigma$ above the typical surface densities around radio AGNs. The value is higher than those for some

spectroscopically confirmed galaxy clusters, e.g., around 7C1756+6520 at $z = 1.41$. The structure around the 6CE1100+3505 was confirmed by spectroscopy using the *HST* WFC3 grism follow up (Noirot et al. 2018). Our study focuses on the star formation properties of possible $z \sim 1.4$ galaxies in this clear 'overdensity' around the 6CE1100+3505.

2.2. WIRCam Observations

The target field was centered at R.A. $= 11^\mathrm{h}30^\mathrm{m}00^\mathrm{s}$ and Dec $= 34^\mathrm{d}44^\mathrm{m}52^\mathrm{s}$ (offset from the coordinates of the radio-loud AGN to avoid the AGN falling on the gaps between the detectors). We observed with the Wide-field InfraRed Camera (WIRCam; Puget et al. 2004) at the Canada France Hawaii Telescope (CFHT) using the filters H (CFHT/WIRCam filter No. 8201) and CH4Off (CFHT/WIRCam filter No. 8204), in the frame of the K-GMT science program (program ID: 15AK005, PI: H. Shim). Most images were obtained during four successive nights in May 2015. Weather conditions were photometric, the seeing ranged between $0.7''$ and $1.3''$. The large field of view of the CFHT/WIRCam ($\sim 20 \times 20\,\mathrm{arcmin^2}$) corresponds to $\sim 10 \times 10\,\mathrm{Mpc^2}$ at the redshift of our targets.

We used the two photometric filters to identify emission from strong Hα lines redshifted to $z \sim 1.4$. The CH4Off filter covers the wavelength range 1.530–$1.630\,\mu\mathrm{m}$ (i.e., has an FWHM bandwidth $\Delta\lambda_\mathrm{MB} = 0.1\,\mu\mathrm{m}$) centered at $1.58\,\mu\mathrm{m}$. This bandwidth is a few times larger than the ones of typical custom narrow-band filters, thus we will refer to this filter as medium-band (hereafter MB) in the following. The H filter used for our broad-band (hereafter BB) observations covers a range of 1.486–$1.776\,\mu\mathrm{m}$ centered at $1.630\,\mu\mathrm{m}$. The bandwidth of the BB filter, $\Delta\lambda_\mathrm{BB} = 0.290\,\mu\mathrm{m}$, is only ~ 3 times larger than that of the MB filter. This limits the detection of Hα emitters to those with the largest Hα ($+$[N II]) equivalent widths.

The MB observation comprises 112 exposures of 48 seconds each, resulting in a total integration time of 90 minutes. The BB imaging achieved a total integration time of 50 minutes, with 200 exposures of 15 seconds each. All frames were obtained in 3×3 dithering mode. For pre-processing we used the 'I'iwi pipeline version 2.1.200 provided by the CFHT (Thanjavur et al. 2011) which includes non-linearity correction, bias subtraction, dark subtraction, flat-fielding, bad pixel masking, and sky subtraction. For MB flux calibration, the WIRCam queued service mode provides magnitude zero points determined from observations of standard stars. Spectrophotometric standards are stars with well-modeled near infrared fluxes, and standard magnitudes are calculated by convolution of filter response function and model spectra. The magnitude zero points are stored in each FITS extension header under the key word PHOT_C0. The values can be different for the four different detectors, thus we used the zero point derived from the pipeline to scale the flux of each detector and each image when combining images to produce the final coadded mosaic. We used *Swarp* (Bertin et al. 2002) to
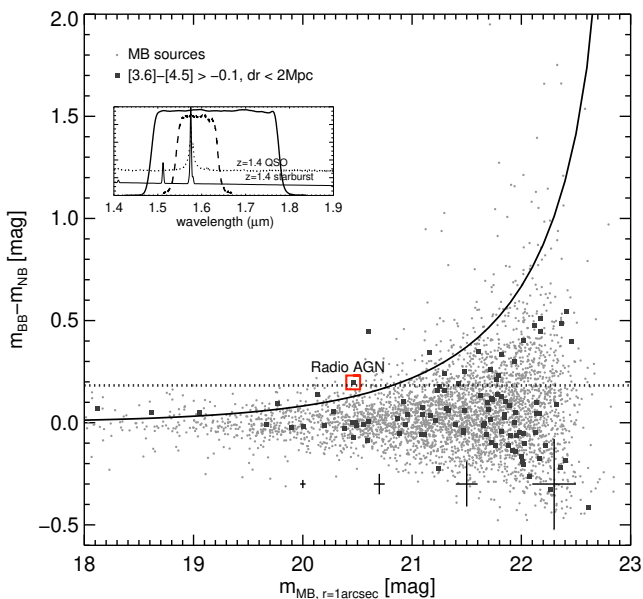
Figure 1. Color–magnitude diagram for sources detected in the medium band (MB) image. The abscissa represents MB magnitude measured in an aperture of radius $1''$, the ordinate indicates the difference between the broad band (BB) and MB magnitudes. The solid line indicates a significance level of $\Sigma = 3$, therefore objects above the solid line are identified as possible line emitters. The radio-loud AGN 6CE 1100+3505 is marked by a red open square. Black filled squares are objects with red IRAC colors ($[3.6] - [4.5] > -0.1$), located within 2 Mpc from the central AGN. The horizontal dotted line indicates the value of Δm ($= m_{\rm BB} - m_{\rm MB}$) which corresponds to the observed equivalent width of 340 Å. Typical magnitude errors for different magnitude bins are indicated by error bars. The inset panel shows the response curves for the CH4Off (MB, dashed line) and H-band (BB, solid line) filters, overplotted with the redshifted Hα emission line of the $z = 1.4$ QSO and starburst model templates.

produce coadded MB and BB images with the 'weighted combine' method, by utilizing the bad pixel mask obtained during the pre-processing as a weight image for inverse variance weighting. A small fraction ($\sim 10\%$ for the MB, $\sim 5\%$ for the BB) of the images are lost due to the poor image quality leading to bad astrometry solutions. The final coadded images and weight images were used for photometric analysis.

3. POTENTIAL LINE EMITTERS

3.1. Photometry

We performed aperture photometry on the reduced and mosaicked images for both filters using an aperture radius of $1''$ (~ 3 pixels). The point spread function (PSF) sizes were similar in both the MB and BB images ($\sim 0.8''$), therefore we did not apply any correction for the PSF difference. We used the dual mode in *SExtractor* (Bertin & Arnouts 1996) for detecting sources (with DETECT_THRESH= 3, i.e., $> 3\sigma$) in the MB image and measuring their fluxes in both the MB and BB images. This way it is also possible to select sources with strong line emission but faint continuum. Such sources might

be spurious if they are only detected in the MB image. Since we do not have multi-wavelength data over this field with depths comparable to the WIRCam images, we removed sources below the $< 3\sigma$ threshold in the BB and MB images to avoid contamination by spurious sources. The 3σ limiting magnitude for an aperture with radius $1''$, estimated from the measured background pixel-to-pixel rms, is 22.5 mag in MB and 23.5 mag in BB.

Before the selection of MB excess objects, star-like objects were removed through cross-comparison to the spectroscopic and photometric star catalog provided by the Sloan Digital Sky Survey (SDSS).

3.2. Selection of MB Excess Objects

The Hα emission line, redshifted to $z \sim 1.4$ (and other strong emission lines at different redshifts redshifted into the MB wavelength range), causes a flux excess in the MB filter compared to the BB filter. We thus used the difference between the MB magnitude ($m_{\rm MB}$) and the BB magnitude ($m_{\rm BB}$) to select potential line emitters. We quantified the statistical significance of a measured flux excess using the parameter Σ (Bunker et al. 1995; Sobral et al. 2013, 2015), where the difference between the counts (i.e., measured flux) in MB ($c_{\rm MB}$) and in BB ($c_{\rm BB}$) should be larger than Σ times the photometric errors for a given aperture size:

$$c_{\rm MB} - c_{\rm BB} > \Sigma \sqrt{\pi r^2 (\sigma_{\rm MB}^2 + \sigma_{\rm BB}^2)} \qquad (1)$$

Here, r indicates the radius of the aperture in pixels (in this study, ~ 3 pixels), $\sigma_{\rm MB}$ and $\sigma_{\rm BB}$ are the rms values of the background in counts per pixel for MB and BB, respectively. In terms of magnitudes ($m_{\rm MB}$ and $m_{\rm BB}$), the parameter Σ can be expressed as

$$\Sigma = \frac{1 - 10^{-0.4(m_{\rm BB} - m_{\rm MB})}}{10^{-0.4(\mathrm{ZP} - m_{\rm MB})} \sqrt{\pi r^2 (\sigma_{\rm MB}^2 + \sigma_{\rm BB}^2)}} \qquad (2)$$

where ZP is the photometric magnitude zero point. Note that after mosaicking, both MB and BB images are scaled to have the same zero point.

The central wavelengths of the MB (1.58 μm) and BB (1.63 μm) filters are slightly different, thus the magnitude difference ($m_{\rm BB} - m_{\rm MB}$) also depends on the color of the stellar continuum. In order to correct this effect, we compared the ($J - H$) and ($m_{\rm BB} - m_{\rm MB}$) colors for bright sources and added the difference to the observed magnitude difference between MB and BB. The J-band magnitudes were derived from the UKIRT Hemisphere Survey data (Dye et al. 2018) which has a 5σ limiting depth of 20.5 AB mag. For objects with no ($J - H$) colors due to the shallow J-band depth, we applied the average correction to the observed ($m_{\rm BB} - m_{\rm MB}$), which is 0.08 mag.

Figure 1 shows the color (i.e., magnitude difference, $m_{\rm BB} - m_{\rm MB}$) as a function of MB magnitude. We classified sources with significance larger than 3 (i.e., $\Sigma > 3$; solid line in the diagram) as potential line emitters. The parameter Σ is basically proportional to the line
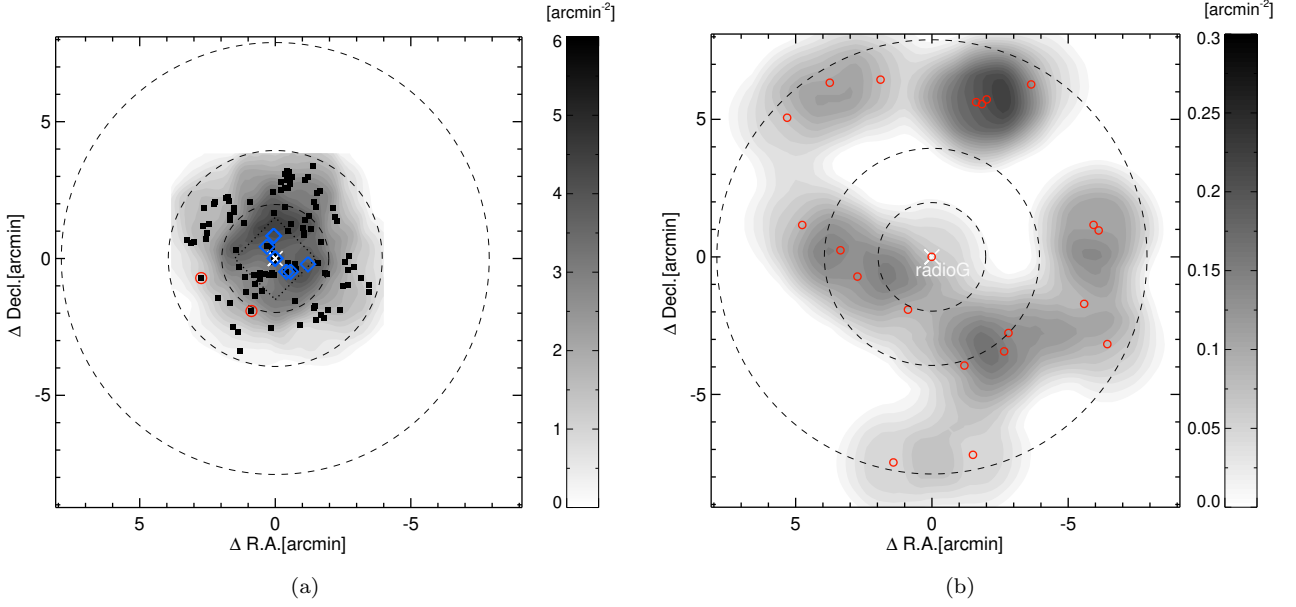
Figure 2. **(a)** Spatial distribution of the IRAC-selected ($[3.6] - [4.5] > -0.1$) objects (filled squares) and spectroscopically confirmed star-forming galaxies at $z \sim 1.44$ (blue diamonds, Noirot et al. 2018). Background contours show the surface density of IRAC-selected objects, on a scale given by the color bar on the right. Only two of the IRAC-selected objects (except the radio AGN itself, marked by an 'X') are identified as strong line emitters based on the MB excess (red open circles). Dashed circles indicate distances of 1 Mpc, 2 Mpc, and 4 Mpc from the central AGN. The dotted line shows the field of view for the WFC3 grism observations. **(b)** Spatial distribution of the MB excess objects with $\Sigma > 3$ (red open circles). The surface density distribution shows no significant excess of strong Hα emitters near the central AGN.

flux, thus the $\Sigma > 3$ cut places a lower limit on the line flux of possible line emitters. In addition to the flux limit, previous studies (e.g., Sobral et al. 2015) have defined a minimum equivalent width (EW) cut in the selection of line emitters because the small photometric errors for bright sources can produce unrealistically large values of Σ. The observed EW is calculated from the magnitude difference and the bandwidths like

$$\text{EW} = \frac{\Delta\lambda_{\text{BB}}\Delta\lambda_{\text{MB}}[1 - 10^{-0.4(m_{\text{BB}}-m_{\text{MB}})}]}{\Delta\lambda_{\text{BB}}10^{-0.4(m_{\text{BB}}-m_{\text{MB}})} - \Delta\lambda_{\text{MB}}} \quad (3)$$

where $\Delta\lambda_{\text{BB}}$ and $\Delta\lambda_{\text{MB}}$ are the bandwidths of the H and CH4Off filters, respectively. We applied the condition $m_{\text{BB}} - m_{\text{MB}} > 0.19$, which is 1.5 times larger than typical color errors at $m_{\text{MB}} = 21.2\,\text{mag}$ ($10\,\sigma$ flux limit), for a robust selection of line emitters. This corresponds to an observed line EW of 340 Å. If the MB flux excess is due to the redshifted Hα (with the contribution from [N II]) at $z \sim 1.4$, the rest-frame EW would be larger than 140 Å. This limit is high compared to the EW(Hα) of local star-forming galaxies, but the EW(Hα) for $z > 1$ star-forming galaxies is found to be larger than that of local galaxies in general (e.g., Fumagalli et al. 2012; Sobral et al. 2013, 2015; Marmol-Queralto et al. 2016). Moreover, though the EW(Hα) for galaxies is not linearly correlated to the Hα line flux, the $z \sim 1$ galaxies with the largest Hα luminosities tend to have EW(Hα) larger than 100 Å (Sobral et al. 2015). The EWs of the selected MB excess objects will be discussed later in Section 4.1, in connection with the flux limit in

our observation.

All except two objects with red IRAC color ($[3.6] - [4.5] > -0.1$, hereafter 'IRAC selected objects') are not classified as MB excess objects as they do not satisfy $\Sigma > 3$ and the EW cut (Figure 1). This shows that the red IRAC colors are sensitive to $z > 1$ galaxies with red rest-frame near-infrared colors, i.e., passive stellar populations.

3.3. Near-infrared Spectroscopy

Near-infrared spectroscopic follow up observations were executed for a limited number of IRAC selected objects and objects detected in the MB image. The observations were made using the MMT and Magellan Infrared Spectrograph (MMIRS) at the MMT observatory, through the K-GMT science program (program ID: MMT-2018A-5, PI: H. Shim). Priority was given to MB bright objects and those with high Σ in the $m_{\text{BB}} - m_{\text{MB}}$ vs. m_{MB} plot in the slit mask configuration stage. Due to instrument scheduling and weather constraints, only one third of the initially allocated time ($\sim 1.5\,\text{hrs}$) was actually executed. The quality of the obtained spectra was relatively poor. Among the 18 objects (6 IRAC-selected objects and 12 MB detected objects; note that not all MB detected objects are MB excess objects, only one of them has $\Sigma > 3$ while the others have Σ between 2 and 3) targeted in the slit mask, only two objects show marginal ($S/N \sim 3$), single emission lines at $1.562\,\mu$m and $1.588\,\mu$m. Note that these objects are those with the brightest in MB or those with the largest significance factor (Σ) among
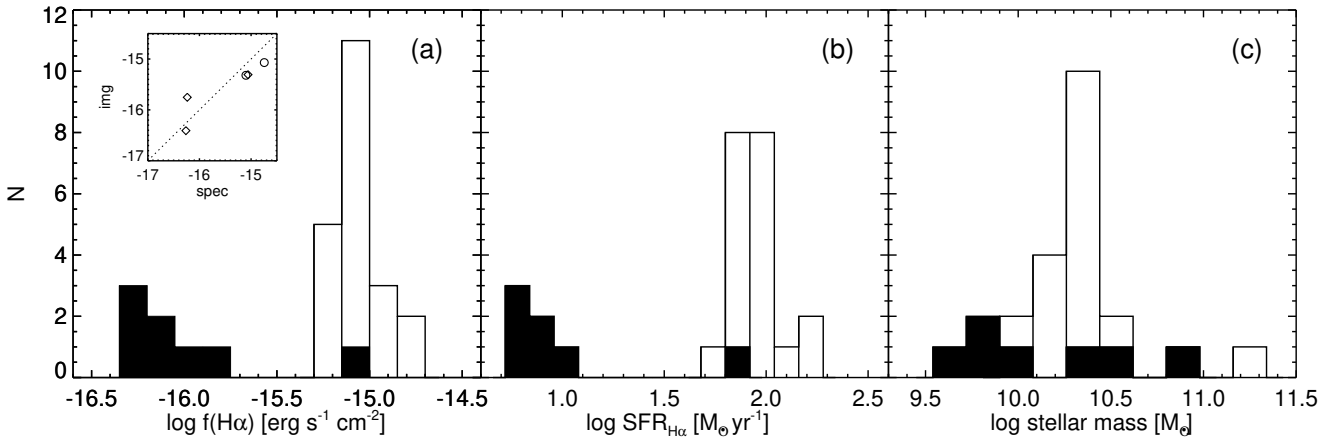
Figure 3. (a) Hα line flux distribution of the MB excess objects found by the CFHT WIRCam observations (open histogram), assuming that these are Hα emitters at $z \sim 1.4$. Line fluxes measured from *HST* WFC/G141 grism spectra are shown by the filled histogram, although these are not identified as MB excess objects. The inset plot shows a comparison of spectroscopic and photometric line fluxes; spectroscopic values are from MMT/MMIRS spectroscopy (circles) and WFC3/G141 grism spectroscopy (diamonds). (b) Star formation rates estimated from Hα line fluxes, assuming a redshift $z = 1.44$ if no spectroscopic redshift is available. Tthe open histogram shows the MB excess objects, the filled histogram shows the values for grism-selected objects. (c) Stellar mass distributions for the MB excess objects (open histogram) and grism-selected objects (filled histogram).

our targets. Since it is difficult to derive spectroscopic redshifts from single emission lines, we used the spectra to derive the line fluxes spectroscopically and compared the values with the line fluxes measured photometrically in Section 4.1.

Recently, Noirot et al. (2018) identified eight cluster member galaxies (including the radio-loud AGN itself) at $z = 1.44$ around 6CE1100+3505 (referred to as CARLA J1103+3449 in their paper) based on *HST*/WFC3 grism observations. For six galaxies, [O III] line emission was detected in addition to Hα, which supports the robustness of the spectroscopic redshift. All confirmed cluster members are located within $\pm 1000\,\mathrm{km\,s^{-1}}$ from the central AGN, thus the structure around this AGN is unlikely to be a massive, virialized cluster. Among the eight spectroscopically confirmed members, four objects are not detected in either of the MB and BB images taken by CFHT/WIRCam, mainly due to their faintness (the $3.6\,\mu$m magnitudes of the objects undetected in BB are $> 1\,$mag fainter than that of the detected objects). The remaining four objects are detected in BB while the central AGN and its interacting companion galaxy are blended in the WIRCam image. Even the objects detected in BB, except the central AGN, do not satisfy our criteria for MB excess objects. Although there is no overlap between the grism-selected cluster members and MB excess objects, we use the grism-selected cluster members to validate the derived photometric line fluxes.

3.4. Contaminants

If the flux excess in the MB is due to strong emission lines redshifted into the MB wavelengths, the possible candidates are (1) strong Paβ line (rest-frame wavelength of $1.282\,\mu$m) emitting galaxies at $z \sim 0.24$, (2) Hα emitting star-forming galaxies at $z \sim 1.4$, (3) [O III]

(+Hβ) line emitters at $z \sim 2.2$, and (4) [O II] line emitters at $z \sim 3.2$. The survey volumes for $z \sim 0.24$ Paβ emitters, $z \sim 1.4$ Hα emitters, $z \sim 2.2$ Hβ + [O III] emitters and $z \sim 3.2$ [O II] emitters are 0.087, 1.67, 2.79, and $3.42 \times 10^5\,\mathrm{Mpc}^3$ respectively considering the filter bandwidths. The expected number of sources of each type in the surveyed area can be calculated by integrating the luminosity function above the detection limit for the line flux density. For the Paβ emitter number density, we used the Hα luminosity function of $z = 0.4$ star-forming galaxies (Sobral et al. 2013) and applied the relative line intensity ratio between hydrogen recombination lines assuming the case B condition (Osterbrock & Ferland 2006). To estimate the number of $z \sim 1.4$ Hα emitters, the luminosity function from Sobral et al. (2013) is used. [O III] and [O II] luminosity functions at $z \sim 2.2$ and $z \sim 3.2$ are from Khostovan et al. (2015). The expected numbers of line emitters of each type are $0.26^{+3.44}_{-0.22}$ for Paβ emitters, $0.53^{+2.87}_{-0.48}$ for [O III] emitters, and $0.0015^{+1.61}_{-0.0005}$ for [O II] emitters while the number of $z \sim 1.4$ Hα emitters is expected to be $33^{+22.4}_{-13.5}$. As the numbers show, the number densities of other line emitters are much smaller than that of the Hα emitters at $z \sim 1.4$, suggesting that most of the MB excess objects sample would consist of Hα line emitters at $z \sim 1.4$.

Contamination by line emitters at different redshifts can be removed by using photometric redshifts or the color-color plane. For example, Khostovan et al. (2015) used $(i - z)$ vs. $(z - K)$ colors and/or $(B - z)$ vs. $(z - K)$ colors to separate [O III] emitters at $z \sim 2.2$ from emitters at different redshifts, and $(U - V)$ vs. $(V - z)$ colors to reliably identify [O II] emitters at $z \sim 3.2$. Despite there being only a limited amount of ancillary multi-wavelength data with limited depth over the 6CE1100+3505 field, we tried to remove the MB excess
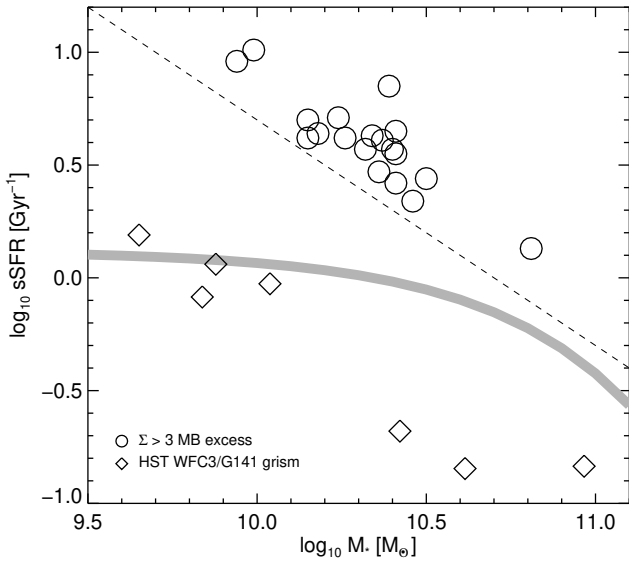
Figure 4. Specific star formation rate (sSFR) vs. stellar mass for MB excess objects (circles) and spectroscopically confirmed $z \sim 1.44$ galaxies from Noirot et al. (2018, diamonds). The dashed line indicates the minimum detectable sSFR as a function of stellar mass, which is given by the depths of the MB and BB images. The grey solid line marks the suggested sSFR–stellar mass relation for $1.2 < z < 1.4$ star-forming main sequence galaxies (Ilbert et al. 2015).

objects possibly located at redshifts other than $z \sim 1.4$ based on the colors and the derived photometric redshifts. First of all, the SDSS provides *ugriz* images over this field. Although the SDSS depths are relatively shallow ($r \sim 22.5$ at 5σ) compared to the WIRCam near-infrared images, we used their $(u - r)$, $(r - z)$, $(i - z)$, and $(z - H)$ colors to exclude objects that satisfy the color-color selection criteria for $z \sim 2.2$ and $z \sim 3.2$ objects from the MB excess sample. Photometric redshifts (z_p) are also available for objects bright enough to be detected in SDSS (Photoz table from the Catalog Archive Server;[1] Beck et al. 2016), so we removed objects with $z_p < 1$ and photometric redshift uncertainty $\delta z_p/(1 + z_p) < 0.05$ from the MB excess sample.

For a limited area (~ 4 arcmin) near the central AGN, deeper *i*-band images (Sloan *i*, ~ 24 mag) are available from the Auxiliary Camera at the William Herschel Telescope (WHT; observed in 2014). Only one object in the initial MB excess sample (with $\Sigma > 3$) is located in the WHT field of view, and the *i*-band magnitude of this object is $m_i = 22.7$ mag. The derived z_p of this object based on the *i*-band, *H*-band, $3.6 \,\mu m$ and $4.5 \,\mu m$ fluxes is $z_p = 1.5$, therefore this object is consistent with being a $z \sim 1.4$ Hα emitter candidate. When only BB and MB photometry is available, we removed sources that are not detected in BB (i.e., *H*-band) since it is impossible to determine whether they are artifacts or strong line emitters with faint continuum. Through visual inspection we removed objects that lie close to the streaks of bright stars since their photometry

is likely to be unreliable.

After the removal of all possible contaminants including artifacts and line emitters at different redshifts, we are left with 20 MB excess objects with $\Sigma > 3$, within 8 arcmin (corresponding to a physical scale of ~ 4 Mpc at $z = 1.44$) from the central AGN. These are likely to be $z \sim 1.4$ galaxies with strong Hα emission. In the HiZELS survey (Sobral et al. 2015), all $z = 0.84$ Hα emitters above the luminosity limit for our sample show rest-frame EWs larger than 140 Å, which is our EW cut limit. Considering the increase of EW as the redshift increases, the EW cut would not reduce the detected sample size. The number of the MB excess objects, 20, is consistent with the expected number of the Hα emitters based on the Hα field galaxy luminosity function within the errors. This is different from the case of $z \sim 2$ protoclusters, where the number density of Hα emitters is a few times that in the field (Hatch et al. 2011).

Figure 2 shows the spatial distribution of the selected galaxies around the central AGN: (a) galaxies with red IRAC colors ($[3.6] - [4.5] > -0.1$) suggested to form an overdensity by Wylezalek et al. (2013) in addition to the spectroscopically confirmed $z \sim 1.44$ star-forming galaxies, and (b) the final sample of MB excess galaxies with $\Sigma > 3$. Unlike the overdense clumps and the east-west alignment of galaxies with red IRAC colors close to the AGN, there are no MB excess galaxies within 1 Mpc from the central AGN. This suggests that there is no contribution by the exceptionally vigorous star-forming galaxies to the overdensity of galaxies at $z \sim 1.44$. Only two galaxies with red IRAC colors turned out to be MB excess objects. More than half of the emission line objects from the *HST* WFC3/G141 grism observations (Noirot et al. 2018) do not show red IRAC color, therefore it appears natural to not detect an MB excess in most of the IRAC selected targets. A rough interpretation, given the limited number of galaxies, is that IRAC color and MB excess select different populations of galaxies at similar redshift: the former selecting relatively quiescent galaxies, the latter selecting active star-forming galaxies.

4. PROPERTIES OF $z \sim 1.4$ Hα EMITTERS
4.1. Hα Line Flux

Assuming the excess in MB over BB is due to the redshifted Hα+[N II] line, the line flux can be estimated from the difference between the BB and MB fluxes and the bandwidths of the filters like

$$f(\text{H}\alpha + [\text{N\textsc{ii}}]) = \frac{\Delta\lambda'_{\text{MB}}(f_{\text{MB}} - f_{\text{BB}})}{1 - \left(\frac{\Delta\lambda_{\text{MB}}}{\Delta\lambda_{\text{BB}}}\right)} \qquad (4)$$

Here, $\Delta\lambda'_{\text{MB}}$ is the bandwidth of the MB filter converted to frequency units; $\Delta\lambda_{\text{MB}}$ and $\Delta\lambda_{\text{BB}}$ are the bandwidths of the MB and BB filters, respectively; and f_{MB} and f_{BB} are fluxes per frequency (f_ν) derived from the observed AB magnitude in each filter. We double-checked the derived line fluxes and the EWs by convolving model spectra with the MB and BB filter response curves, with

---

Table 1
List of medium band excess objects

R.A.	Dec.	$m_{\rm MB}$ (mag)	$m_{\rm BB}$ (mag)	Σ	$\log f(\rm H\alpha)$ (erg s^{-1} cm^{-2})	EW$_{\rm obs}$ (Å)	dr (Mpc)
11 03 30.4	+34 47 51	20.60 ± 0.04	21.13 ± 0.05	7.97	-14.77	845	1.070
11 03 39.5	+34 49 04	21.16 ± 0.07	21.59 ± 0.09	3.82	-15.07	535	1.432
11 03 42.5	+34 50 01	22.26 ± 0.19	23.34 ± 0.27	3.10	-15.10	7194	1.706
11 03 12.5	+34 47 00	20.90 ± 0.06	21.18 ± 0.07	2.96	-15.21	231	1.998
11 03 20.3	+34 45 50	21.22 ± 0.09	21.69 ± 0.09	3.91	-14.95	640	2.091
11 03 13.2	+34 46 20	20.68 ± 0.05	21.00 ± 0.07	4.20	-15.08	299	2.199
11 03 49.3	+34 50 56	21.81 ± 0.15	22.49 ± 0.20	3.26	-15.16	1444	2.482
11 02 58.9	+34 48 04	21.03 ± 0.07	21.43 ± 0.10	3.94	-15.03	449	2.961
11 03 17.2	+34 55 20	21.80 ± 0.17	23.16 ± 0.26	5.51	-15.00	25805	2.965
11 03 18.2	+34 55 24	21.17 ± 0.09	21.57 ± 0.12	3.43	-15.03	439	2.967
11 02 57.3	+34 50 56	21.83 ± 0.16	22.48 ± 0.25	3.05	-15.18	1274	3.063
11 03 16.4	+34 55 30	21.21 ± 0.10	21.58 ± 0.13	3.05	-15.18	410	3.074
11 02 56.3	+34 50 44	21.74 ± 0.14	22.34 ± 0.20	3.17	-15.13	1121	3.139
11 03 35.3	+34 56 13	21.51 ± 0.17	22.02 ± 0.28	3.34	-15.13	787	3.403
11 02 54.8	+34 46 36	21.26 ± 0.09	21.70 ± 0.10	3.55	-15.04	555	3.636
11 03 08.4	+34 56 03	21.33 ± 0.15	21.78 ± 0.18	3.35	-15.11	565	3.674
11 03 52.0	+34 54 50	20.92 ± 0.09	21.47 ± 0.12	6.02	-14.77	883	3.718
11 03 18.8	+34 42 35	21.13 ± 0.07	21.48 ± 0.09	3.05	-15.18	353	3.725
11 03 44.4	+34 56 06	20.72 ± 0.08	21.02 ± 0.10	3.75	-15.06	246	3.729
11 03 33.0	+34 42 18	21.56 ± 0.10	22.11 ± 0.14	3.39	-15.06	902	3.854

emission lines of varying flux density added, to reproduce the observed (BB–MB) colors. The derived $f(\rm H\alpha+[N\,II])$ should be corrected for the contribution from [N II] to isolate $f(\rm H\alpha)$. It has been suggested that the line flux ratio [N II]/Hα depends on the rest-frame Hα+[N II] EW (Sobral et al. 2015), with smaller contributions by [N II] in galaxies with large EWs. For the limiting EW of 140 Å in our study, the [N II]/Hα ratio is expected to be ~ 0.17. The line fluxes derived from MB and BB photometry are corrected for the [N II] contribution using the [N II]/Hα ratio-vs.-EW relation. We applied aperture correction to the derived line fluxes because the aperture radius of 1 arcsec we used for the identification of MB excess objects requires a non-negligible aperture correction to derive total magnitudes. The aperture correction factors were consistent in MB and BB within 10 %, thus we used the aperture correction factors of the MB data to correct the Hα line fluxes. From the growth curves of isolated sources, the aperture correction factors are in the range 1.1–1.8 to scale fluxes within the 1″ aperture to total fluxes, with a dependence on the FWHM of the objects. Most of the Hα emitters are not significantly extended, thus the aperture corrections applied to their $f(\rm H\alpha)$ were 1.1–1.3.

Figure 3a shows the Hα line flux distribution of the MB excess objects. The minimum $f(\rm H\alpha)$ that can be measured in our analysis is determined by the Σ factor, with $\Sigma = 3$ roughly corresponding to 4.9×10^{-16} erg s^{-1} cm^{-2} which in turn corresponds to a luminosity of $L(\rm H\alpha) > 6 \times 10^{42}$ erg s^{-1} at $z \sim 1.4$. If the [N II]/Hα ratio is 0.17 and the aperture correction factor is 1.1, the line flux limit is $> 4.6 \times 10^{-16}$ erg s^{-1} cm^{-2}. We compared the Hα line flux measured from the spectrum to the line flux estimated from the MB excess (see

inset plot in Figure 3a). Both the photometric line flux and the spectroscopic line flux are aperture corrected considering the photometric apertures and slit widths in case of the *MMT*/MMIRS observation, but not corrected for [N II] since the [N II] and Hα lines were not resolved by the grism. Though the number of the galaxies is small (five in total, including the radio-loud AGN), the overall consistency between the spectroscopically measured line flux and photometrically estimated line flux validates our use of line fluxes for the derivation of star formation rates in the next section. The derived $f(\rm H\alpha)$, observed EW(Hα+[N II]), and the cluster-centric distance of all 20 MB excess objects within < 4 Mpc from the AGN are listed in Table 1.

4.2. Star Formation Rate and Stellar Mass

The star formation rates of the potential Hα emitters are derived from the Hα line luminosity, following the equation from Kennicutt (1998),

$$\mathrm{SFR}[M_\odot\ \mathrm{yr}^{-1}] = 7.9 \times 10^{-42} L(\mathrm{H\alpha})[\mathrm{erg\ s}^{-1}] \qquad (5)$$

As expected from the high $f(\rm H\alpha)$ limit, SFRs for objects identified by their MB excess are higher than $50\,M_\odot$ yr^{-1} (Figure 3b). Note that the SFR presented here represents the lower limit of true star formation since dust attenuation is not considered. The SFRs of the MB excess objects are in the range of 50–300 $M_\odot$ yr^{-1}. A statistical correlation between the $A(\rm H\alpha)$ and the SFR (and the stellar mass) is known for local galaxies (Garn & Best 2010), thus by applying this relation, the intrinsic SFR can be as high as 100–600 $M_\odot$ yr^{-1}. Such a range in SFR is close to that of dusty star-forming galaxies, which in general are used as probes of galaxy overdensities at $z > 2$.

Galaxy evolution can be affected by environment, but the parameter that drives the evolution most is mass. Therefore we estimated the stellar masses of MB excess objects as well, using the rest-frame near-infrared magnitudes. To estimate the stellar mass of a galaxy, we used its IRAC $3.6\,\mu m$ flux (rest-frame $\sim 1.4\,\mu m$ at $z \sim 1.4$) and applied the average M/L ratio in the near-infrared (Bell & de Jong 2001; Bell et al. 2003) which is rather independent of galaxy type. A slow evolution of M/L ratio with redshift, especially in early-type galaxies, is expected (van der Wel et al. 2005), yet the effect was not taken into account here since the line emitters are considered to be young galaxies. Where $3.6\,\mu m$ fluxes were not available due to the limited IRAC field of view and its layout, we used $4.5\,\mu m$ fluxes instead. If none of the IRAC bands was available, we applied a linear relation between the H-band magnitude and the $\log M_*$ which was derived from the $3.6\,\mu m$-detected MB excess objects. All magnitudes in $3.6\,\mu m$, $4.5\,\mu m$, and H-band were aperture corrected to derive stellar masses. Figure 3c shows the derived stellar mass distribution. Most of the MB excess objects have stellar masses of a few $\times 10^{10}\,M_\odot$, while the H-band magnitude limit places the stellar mass limit at $> 10^{10}\,M_\odot$ when IRAC data are not available. The stellar masses of MB excess objects are comparable to those of confirmed $z = 1.44$ star-forming galaxies from Noirot et al. (2018).

4.3. Comparison to Main Sequence Galaxies

As shown in Figure 2, none of the $\Sigma > 3$ MB excess objects is located within $1\,Mpc$ from the central AGN. The smoothed surface density distribution of IRAC color-selected galaxies shows an overdensity in the proximity of the AGN, but the peak of the surface density distribution of MB excess objects is not consistent with that of the IRAC color-selected objects or that of the grism selected $z \sim 1.4$ galaxies. In short, we see that the possible 'structure' associated with 6CE1100+3505 does *not* host galaxies with SFR $> 50\,M_\odot\,yr^{-1}$. The absence of vigorous starbursts is expected from the absence of an excess in the number density of $H\alpha$ emitters in this structure compared to the field (Section 3.4). Several $z > 2$ proto-clusters around radio galaxies show an excess of $H\alpha$ emitters (Hatch et al. 2011; Shimakawa et al. 2018) or have ultra-luminous infrared galaxies near their centers (Cooke et al. 2014). On the contrary, the lack of enhanced star formation in the structure at $z \sim 1.4$ studied here shows that an overdense environment does not anymore trigger vigorous star formation, though the reason for this – environmental quenching or galaxy feedback – is unclear.

Figure 4 shows the relation between the specific star formation rate (sSFR) and the stellar mass of MB selected galaxies. Since there is a line flux limit, i.e., a limit on the SFR down to which $H\alpha$ emission can be detected via the MB excess, the MB excess selection is biased to high sSFR objects at low stellar mass and low sSFR objects at high stellar mass. The selection bias naturally arises from our significance cut, since the criteria illustrated in Figure 1 select objects with

ever larger EW at fainter magnitudes. The sSFR limit for different stellar masses of galaxies is marked by a dashed line in Figure 4. The MB excess objects show sSFR at least $0.5\,dex$ to $1.0\,dex$ higher than that of star-forming main sequence galaxies, therefore these should be considered as starbursts. As we have discussed in the context of the spatial distribution (Figure 2), these extreme starbursts do not seem to be associated with the known protocluster. Only galaxies with stellar masses higher than $5 \times 10^{10}\,M_\odot$ can be probed down to $\log(sSFR) \sim 0\,[Gyr^{-1}]$, which is close to the star-forming main sequence. None of the galaxies within $1\,Mpc$ from the central AGN is found to be located above the main sequence. Massive galaxies confirmed to be at $z \sim 1.44$ show sSFRs $\sim 1\,dex$ lower than the main sequence, showing the efficient star formation quenching due to the environment.

The structure around 6CE1100+3505 is classified as probable cluster in Noirot et al. (2018), but from estimates of the significance of the spectroscopic overdensity and the galaxy contrast from the background, they also suggested that this structure might be a 'node' of the cosmic web. The velocity dispersion of the spectroscopically confirmed members within $1\,Mpc$ implies that the mass of this structure is $\sim 10^{14}\,M_\odot$. At this mass scale, it is probable that the cluster is not virialized and galaxies or groups of galaxies are falling into the cluster along filamentary structures. However, even with a present infall of galaxies, the star formation in those galaxies is too low to be detected in our observations which are sensitive to SFR on scales comparable to that of dusty star-forming galaxies.

5. SUMMARY

We investigated the overdensity around the radio-loud AGN 6CE1100+3505 at $z = 1.44$ using near-infrared medium band and broad band imaging observations. The overdensity has been already been confirmed spectroscopically to be a probable cluster with a relatively small velocity dispersion. Our shallow MB and BB observations enable the selection of MB excess objects with exceptionally large emission line fluxes. Assuming that the origin of the MB excess is the $H\alpha$ line redshifted to $z \sim 1.4$, we identified 20 possible $H\alpha$ line emitters with $H\alpha$ line flux larger than $4.9 \times 10^{-16}\,erg\,s^{-1}\,cm^{-2}$ within $4\,Mpc$ from the central AGN. The MB excess objects are thought to be galaxies with SFRs as large as 50–$300\,M_\odot\,yr^{-1}$ and stellar masses of a few times $10^{10}\,M_\odot$. The specific star formation rates of these galaxies are up to $1\,dex$ higher than those of star-forming main sequence galaxies of the same stellar mass, considering the mean dust attenuation.

Interestingly, there are no such extreme galaxies within $1\,Mpc$ from the AGN. Previous studies using HST/WFC3 grism observations of the very center of the structure found galaxies with SFRs less than $10\,M_\odot\,yr^{-1}$ with stellar masses $3 \times 10^9 - 10^{11}\,M_\odot$. The sSFRs of galaxies associated with the $z \sim 1.44$ structure (which has a mass above $2 \times 10^{10}\,M_\odot$) are lower than those of star-forming main-sequence galaxies by $\sim 1\,dex$. In ad-

dition to the results from previous studies, our search of MB excess objects confirms the lack of strong starbursts related to the $z \sim 1.4$ cluster, different from the case of galaxy overdensities at $z > 2$.

REFERENCES

Alberts, S., Pope, A., Brodwin, M., et al. 2014, The Evolution of Dust-obscured Star Formation Activity in Galaxy Clusters relative to the Field over the Last 9 Billion Years, MNRAS, 437, 437

Bai, L., Rieke, G. H., Rieke, M. J., Christlein, D., & Zabludoff, A. I., 2009, The Infrared Luminosity Functions of Rich Clusters, ApJ, 639, 1840

Bayliss, M. B., Ashby, M. L. N., Ruel, J., et al. 2014, SPT-CL J2040-4451: An SZ-selected Galaxy Cluster at $z = 1.478$ with Significant Ongoing Star Formation, ApJ, 794, 12

Beck, R., Dobos, L., Budavári, T., Szalay, A. S., & Csabai, I., 2016, Photometric Redshifts for the SDSS Data Release 12, MNRAS, 460, 1371

Bell, E. F., de Jong, R. S. 2001, Stellar Mass-to-Light Ratios and the Tully-Fisher Relation, ApJ, 550, 212

Bell, E. F., McIntosh, D. H., Katz, N., & Weinberg, M. D. 2003, The Optical and Near-Infrared Properties of Galaxies. I. Luminosity and Stellar Mass Functions, ApJS, 149, 289

Bertin, E., & Arnouts, S. 1996, SExtractor: Software for Source Extraction, A&AS, 117, 393

Bertin, E, Mellier, Y., Radovich, M., et al. 2002, The TERAPIX Pipeline, ASP Conf. Ser., 281, 228

Brodwin, M., Stanford, S. A., Gonzalez, A. H., et al. 2013, The Era of Star Formation in Galaxy Clusters, ApJ, 779, 138

Bunker, A. J., Warren, S. J., Hewett, P. C., & Clements, D. L., 1995, On Near-infrared $H\alpha$ Searches for High-redshift Galaxies, MNRAS, 273, 513

Chung, S. M., Eisenhardt, P. R., Gonzalez, A. H., et al. 2011, A WISE View of Star Formation in Local Galaxy Clusters, ApJ, 743, 34

Clements, D. L., Braglia, F., Petitpas, G., et al. 2015, H-ATLAS: A Candidate High Redshift Cluster/Protocluster of Star-forming Galaxies, MNRAS, 461, 1719

Cooke, E. A., Hatch, N. A., Muldrew, S. I., et al. 2014, A $z = 2.5$ Protocluster Associated with the Radio Galaxy MRC 2104-242: Star Formation and Differing Mass Functions in Dense Environments, MNRAS, 2014, 440, 3262

Dannerbauer, H., Kurk, J. D., De Breuck, C., et al. 2014, An Excess of Dusty Starbursts Related to the Spiderweb Galaxy, A&A, 570, 55

Darvish, B., Mobasher, B., Sobral, D., et al. 2016, The Effects of the Local Environment and Stellar Mass on Galaxy Quenching to $z \sim 3$, ApJ, 825, 113

Davies, J. I., Baes, M., Bendo, G. J., et al. 2010, The Herschel Virgo Cluster Survey. I. Luminosity Function, A&A, 518, 48

Dressler, A. 1980, Galaxy Morphology in Rich Clusters – Implications for the Formation and Evolution of Galaxies, ApJ, 236, 351

Dye, S., Lawrence, A., Read, M. A., et al. 2018, The UKIRT Hemisphere Survey: Definition and J-band Data Release, MNRAS, 473, 5113

Elbaz, D., Daddi, E., Le Borgne, D., et al. 2007, The Reversal of the Star Formation–Density Relation in the Distant Universe, A&A, 468, 33

Fumagalli, M., Patel, S. G., Franx, M., et al. 2012, $H\alpha$ Equivalent Widths from the 3D-HST Survey: Evolution with Redshift and Dependence on Stellar Mass, ApJL, 757, 22

Garn, T. & Best, P. N. 2010, Predicting Dust Extinction from the Stellar Mass of a Galaxy, MNRAS, 409, 421

Geach, J. E., Smail, I., Ellis, R. S., et al. 2006, A Panoramic Mid-Infrared Survey of Two Distant Clusters, ApJ, 649, 661

Hatch, N. A., Kurk, J. D, Pentericci, L., et al. 2011, $H\alpha$ Emitters in $z \sim 2$ Protoclusters: Evidence for Faster Evolution in Dense Environments, MNRAS, 415, 2993

Hayashi, M., Kodama, T., Koyama, Y., et al. 2010, High Star Formation Activity in the Central Region of a Distant Cluster at $z = 1.46$, MNRAS, 402, 1980

Ilbert, O., Arnouts, S., Le Floc'h, E., et al. 2015, Evolution of the Specific Star Formation Rate Function at $z < 1.4$ – Dissecting the mass-SFR plane in COSMOS and GOODS, A&A, 579, 2

Iglesias-Paramo, J., Boselli, A., Cortese, L., Vilchez, J. M., & Gavazzi, G., 2002, A Deep $H\alpha$ Survey of Galaxies in the Two Nearby Clusters Abell 1367 and Coma. The $H\alpha$ Luminosity Functions, A&A, 384, 383

Kauffmann, G., White, S. D. M., Heckman, T. M., et al. 2004, The Environmental Dependence of the Relations between Stellar Mass, Structure, Star Formation and Nuclear Activity in Galaxies, MNRAS, 353, 713

Kennicutt, R. C. Jr., 1998, Star Formation in Galaxies Along the Hubble Sequence, ARA&A, 36, 189

Khostovan, A. A., Sobral, D., Mobasher, B., et al. 2015, Evolution of the $H\beta$+[O III] and [O II] Luminosity Functions and the [O II] Star Formation History of the Universe up to $z \sim 5$ from HiZELS, MNRAS, 452, 3948

Lee, S.-K., Im, M., Kim, J.-W., et al. 2015, Evolution of Star-formation Properties of High-redshift Cluster Galaxies since $z = 2$, ApJ, 810, 90

Ma, C.-J., Smail, I., Swinbank, A. M., et al. 2015, Dusty Starbursts and the Formation of Elliptical Galaxies: A SCUBA-2 Survey of a $z = 1.46$ Cluster, ApJ, 806, 257

Mármol-Queraltó, E., McLure, R. J., Cullen, F., et al. 2016, The Evolution of the Equivalent Width of the $H\alpha$ Emission Line and Specific Star Formation Rate in Star-forming Galaxies at $1 < z < 5$, MNRAS, 460, 3587

Miller, T. B., Hayward, C. C., Chapman, S. C., et al. 2015, The Bias of the Submillimetre Galaxy Population: SMGs are Poor Tracers of the Most-massive Structures in the $z \sim 2$ Universe, MNRAS, 452, 878

Nantais, J. B., Muzzin, A., van der Burg, R. F. J., et al. 2017, Evidence for Strong Evolution in Galaxy Environmental Quenching Efficiency between $z = 1.6$ and $z = 0.9$, MNRAS, 465, 104

Noirot, G., Stern, D., Mei, S., et al. 2018, HST Grism Confirmation of 16 Structures at $1.4 < z < 2.8$ from the Clusters Around Radio-Loud AGN (CARLA) Survey, 2018, ApJ, 859, 38

Osterbrock, D. E., & Ferland, G. J., 2006, Astrophysics of Gaseous Nebulae and Active Galactic Nuclei (Sausalito, CA: University Science Books)

Papovich, C., Rudnick, G., Le Floc'h, E., et al. 2007, Spitzer Mid- to Far-Infrared Flux Densities of Distant Galaxies, ApJ, 668, 45

Puget, P., Stadler, E., Doyon, R., et al. 2004, WIRCam: The Infrared Wide-field Camera for the Canada-France-Hawaii Telescope, Proc. SPIE, 5492, 978

Santos, J. S., Altieri, B., Popesso, P., et al. 2013, Dust-obscured Star Formation in the Outskirts of XMMU J2235.3-2557, a Massive Galaxy Cluster at $z = 1.4$, MN-RAS, 433, 1287

Sawicki, M., 2002, The 1.6 Micron Bump as a Photometric Redshift Indicator, AJ, 124, 3050

Shimakawa, R., Kodama, T., Hayashi, M., et al. 2018, MA-HALO Deep Cluster Survey I. Accelerated and Enhanced Galaxy Formation in the Densest Regions of a Protocluster at $z = 2.5$, MNRAS, 473, 1977

Sobral, D., Smail, I., Best, P. N., et al. 2013, A Large Hα Survey at $z = 2.23$, 1.47, 0.84 and 0.40: The 11 Gyr Evolution of Star-forming Galaxies from HiZELS, MNRAS, 428, 1128

Sobral, D., Matthee, J., Best, P. N. et al. 2015, CF-HiZELS, an $\sim 10\,\mathrm{deg}^2$ Emission-line Survey with Spectroscopic Follow-up: Hα, [O III] + Hβ and [O II] Luminosity Functions at $z = 0.8$, 1.4 and 2.2, MNRAS, 451, 2303

Stach, S. M., Swinbank, A. M., Smail, I., et al. 2017, ALMA Pinpoints a Strong Overdensity of U/LIRGs in the Massive Cluster XCS J2215 at $z = 1.46$, ApJ, 849, 154

Strazzullo, V., Pannella, M., Mohr, J. J., et al. 2019, Galaxy Populations in the Most Distant SPT-SZ Clusters – I. Environmental Quenching in Massive Clusters at $1.4 \leq z < 1.7$, A&A, 622, 117

Thanjavur, K., Teeple, D., & Yan, C.-H. 2011, CFHT Data Processing and Calibration Pipeline for WIRCam: Iiwi (near-IR imaging), in: Telescopes from Afar, eds. S. Gajadhar, J. Walawender, R. Genet, et al., 72

Umehata, H., Tamura, Y., Kohno, K., et al. 2015, ALMA Deep Field in SSA22: A Concentration of Dusty Starbursts in a $z = 3.09$ Protocluster Core, ApJL, 815, 8

van der Wel, A., Franx, M., van Dokkum, P. G., et al. 2005, Mass-to-Light Ratios of Field Early-Type Galaxies at $z \sim 1$ from Ultradeep Spectroscopy: Evidence for Mass-dependent Evolution, ApJ, 631, 145

Wagner, C. R., Courteau, S., Brodwin, M., et al. 2017, The Evolution of Star Formation Activity in Cluster Galaxies over $0.15 < z < 1.5$, ApJ, 834, 53

Wylezalek, D., Galametz, A., Stern, D., et al. 2013, Galaxy Clusters around Radio-loud Active Galactic Nuclei at $1.3 < z < 3.2$ as Seen by Spitzer, ApJ, 769, 79